

Hydration Mechanism and Microstructure Regulation of CNGA All-Solid-Waste Cementitious Material

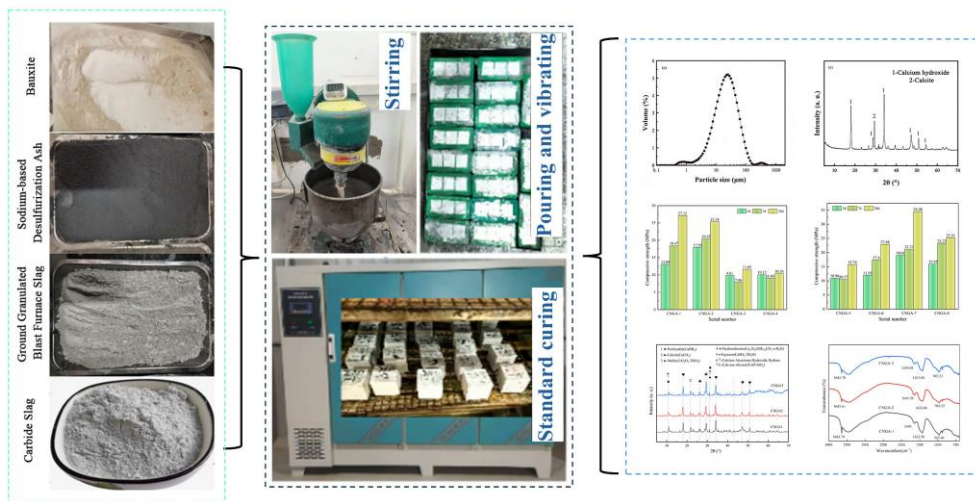
Yannian Zhang^a, Qiyue Ren^a, Yingliang Tan^{a,*}, Qingjie Wang^a, Moncef L. Nehdi^b, Shunshan Zhang^c

^a School of Transportation Engineering, Dalian Jiaotong University, Dalian 116028, China

^b College of Engineering and Physical Sciences, University of Guelph, Guelph N1G 2W1, Canada

^c Beijing Building and Apartment Section, China State Railway Beijing Bureau Group Co., Ltd., Beijing 100010, China

Graphic Abstract



CNGA All-Solid-Waste Cementitious Material

Highlights

1. Directionally formed Aft in CNGA interpenetrates C-S-H gel, forming a gel-crystal composite structure as the material's main strength source.
2. CS and NDA achieve alkali source functional division (rapid elevation, long-term retention) through dual-alkaline synergistic activation.
3. The strength contribution of CS manifests in two key aspects: alkaline activation and latent cementitious properties.
4. Optimal NDA dosage balances alkaline activation while inhibiting byproducts (e.g., CaCO_3 , gypsum).
5. BA contributes by synergistically optimizing the reaction system for an intertwined spatial network, plus supplementary support.

20 Abstract

21 To enhance the alkalinity stability of industrial solid wastes during activation, optimize hydration products, and
22 refine microstructure, an all-solid-waste cementitious material (CNGA) was developed in this study. Ground
23 granulated blast furnace slag (GGBS) and bauxite (BA) were used as precursors, while carbide slag (CS) and
24 sodium-based desulfurization ash (NDA) served as dual-alkaline solid waste activators to replace industrial strong
25 alkalis. By systematically adjusting the mix proportion of alkaline solid wastes, NDA dosage, BA dosage, and water-
26 to-binder ratio, the macroscopic mechanical properties were evaluated through compressive strength tests, and the
27 hydration mechanism was investigated using XRD, FTIR, and SEM-EDS. The results indicate that CS–NDA dual-
28 alkaline synergistic activation enables a functional division of rapid alkali elevation and long-term alkali retention,
29 thereby ensuring continuous hydration and suppressing by-product formation. An appropriate NDA dosage
30 significantly enhances the early-age reactivity of GGBS and BA, with an optimal content of 2% achieving a balance
31 between alkaline activation, C–S–H gel formation, and inhibition of side reactions. Furthermore, BA incorporation
32 supplies reactive Al₂O₃, promoting ettringite (AFt) formation and contributing to the generation of C–A–H gel. The
33 SO₄²⁻ in NDA facilitates directional AFt formation, which enhances early-age strength and promotes the
34 development of a gel–crystal composite microstructure.

35 **Keywords:** All-solid-waste cementitious materials; Alkali-activated materials; Dual-alkaline solid waste synergistic
36 activation; Gel-crystal composite structure; Hydration products

37 1. Introduction

38 The cement industry contributes 8–10% of global anthropogenic CO₂ emissions and depends heavily on non-
39 renewable resources such as limestone and clay, posing sustainability challenges [1-3]. In this context, Alkali-
40 Activated Materials have emerged as a promising alternative to Portland cement due to their low carbon footprint
41 and high resource utilization [4]. AAMs based on industrial solid wastes such as GGBS and fly ash enable high-
42 value waste utilization while significantly reducing emissions [5, 6]. However, existing studies mainly emphasize
43 basic performance and single-system optimization, and from an engineering and high-performance perspective,
44 AAMs still face key bottlenecks in application and performance optimization that limit large-scale use [7, 8]. Firstly,
45 traditional AAMs rely on high-energy, corrosive chemical alkalis such as NaOH and Na₂SiO₃ as activators. This
46 increases production cost and safety risks, and under high alkalinity exacerbates drying shrinkage, induces late-age
47 strength loss, raises chloride penetration risk, and compromises long-term durability. [9, 10]. Secondly, chemically
48 synthesized strong alkalis account for 52%–58% of the total cost of conventional two-component AAMs with a 1:2
49 NaOH–sodium silicate mix. Sodium silicate alone contributes 35%–40% due to its high energy consumption and

* Corresponding author.

Email: tanyingliang@djtu.edu.cn

50 unit price of about 380 USD per ton, and their combined share exceeds 50%, far higher than that of alkaline solid
51 waste activators. [11]. Moreover, the high-alkaline environment deteriorates paste fluidity, requiring the additional
52 addition of polycarboxylate superplasticizers to meet construction requirements [12]. Therefore, it is essential to
53 develop alkaline solid waste activation systems without external strong alkalis, to enable low-carbon and large-scale
54 application of AAMs while achieving high-value synergistic utilization of multiple industrial solid wastes.

55 In recent years, significant progress has been made in solid waste-based alkali-activated systems, with researchers
56 incorporating multiple solid wastes such as carbide slag, sodium-based desulfurization ash, and GGBS into
57 composite cementitious systems. Tripathy et al.[13] found that sodium-based components such as Na^+ increase
58 system alkalinity, accelerate depolymerization of the silico-aluminum network in GGBS, and promote formation of
59 C-(A)-S-H gel, supporting the use of sodium-containing solid wastes such as NDA and soda residue as activation
60 aids. Zheng et al.[14] successfully applied solid sodium silicate to soft soil stabilization, verifying the feasibility of
61 solid alkali activators in engineering practice. Guo et al. [15] further discovered that the synergistic activation of SR
62 and CS can effectively replace strong alkalis such as NaOH, reducing preparation costs; the experiment introduced
63 NDA to rapidly increase initial alkalinity, which significantly promoted early-age hydration reactions. Gu et al.[16]
64 confirmed that the synergy between CS and desulfurization ash effectively supplies Ca^{2+} , OH^- , and SO_4^{2-} to
65 accelerate GGBS hydration, providing valuable insights for solid waste-based activation systems. In addition to
66 studies on alkaline activators, extensive research has also been conducted on the microstructure and hydration
67 products of solid waste-based alkali-activated materials. Marvila et al.[17] systematically investigated the effects of
68 curing regimes and Na_2O concentration on the mechanical properties of alkali-activated cement using ground
69 granulated blast furnace slag as the precursor, and noted that C-S-H gel is the main source of strength development,
70 laying an important foundation for understanding the role of silicate gel in GGBS-based systems. Wang et al.[18]
71 prepared a low-alkali system with a 14-day compressive strength of 45.17 MPa by blending desulfurization gypsum,
72 GGBS, and fly ash; Xu et al.[19] successfully developed clinker-free concrete using SR, GGBS, steel slag, and
73 desulfurization gypsum, achieving a 28-day compressive strength of 38.33 MPa and verifying the feasibility of
74 synergistic utilization of multiple industrial solid wastes. Seo et al.[20] demonstrated that the main hydration
75 products of the CS-ground granulated blast furnace slag binary system are C-A-S-H gel, AFt, and hydrotalcite-like
76 phases, with system strength and pore structure regulated by component ratios. Wang et al.[21] reported that using
77 bauxite tailings and GGBFS as precursors in composite cementitious systems alters the Al/Si ratio, increases
78 hydration product content, and enhances structural complexity and density. These findings provide an important
79 basis for industrial solid waste utilization. However, further analysis indicates that despite progress in single solid
80 waste activation and partial multi-solid waste synergistic activation, significant common bottlenecks remain, as
81 outlined below: (1) Under high sodium-based content conditions, various secondary reactions may occur in the
82 system: for instance, excess SO_4^{2-} may combine with Ca^{2+} to form excessive AFt, leading to volume expansion
83 exceeding the material's bearing capacity and thus damaging the material structure [22]; Na^+ can not only react with
84 CO_2 in the environment to form Na_2CO_3 [23] but also combine with SO_4^{2-} to generate Na_2SO_4 , inducing salt

85 crystallization pressure during wet-dry cycles [24, 25]. Therefore, the optimal dosage range of sodium-based
86 components and their regulatory effect on the composition of hydration products require further clarification.
87 Furthermore, the massive formation of these non-cementitious phases may consume effective calcium sources in
88 the system and affect the pore structure, thereby exerting potential impacts on the formation of C-S-H gel and
89 mechanical properties[26, 27]. Consequently, the system not only needs a sustained and stable alkaline environment
90 but also requires GGBS, steel slag, and other materials as main silico-aluminum sources to promote the formation
91 of cementitious phases [28, 29]. (2) Although solid sodium silicate effectively promotes the initiation of
92 cementitious reactions through an initial high-alkaline environment, its rapid dissolution during hydration may lead
93 to a significant attenuation of system alkalinity over time, making it difficult to maintain a long-term stable high pH
94 environment [14]. (3) The chemical composition of SR is usually complex, often containing Na_2CO_3 or residual
95 NaOH, and its alkalinity release behavior is greatly influenced by environmental factors [22, 30]; meanwhile, the
96 content of reactive aluminum in GGBS and steel slag is relatively limited, which may pose challenges to the precise
97 regulation of the Al/Si ratio and degree of network polymerization in C-(A)-S-H gel [23, 26, 31]. Therefore,
98 introducing aluminum-rich components (e.g., bauxite (BA)) into all-solid-waste cementitious materials and
99 constructing an endogenous, stable alkali activation mechanism may further optimize the hydration product
100 structure and enhance the controllability of material properties [14, 31]. Li et al.[32] confirmed that the CS-GGBS
101 binary system lacks sulfate and aluminum-rich components, hindering SO_4^{2-} -mediated Aft formation and Al^{3+} -
102 induced cross-linking of the C-S-H network, thus preventing development of a gel-crystal synergistic
103 microstructure. Although these studies provide a foundation for solid-waste utilization, key limitations remain,
104 including unclear regulation of sodium-based components, poor long-term alkalinity stability, and difficulty forming
105 gel-crystal structures due to insufficient aluminum-rich phases, all of which restrict performance optimization and
106 large-scale application. Therefore, expanding component design and introducing multifunctional solid wastes to
107 regulate multiphase hydration products is essential to overcome these challenges.

108 This study develops a CS-NDA-GGBS-BA CNGA all-solid-waste cementitious material using GGBS and BA as
109 precursors and CS and NDA as activators. Four variable groups including NDA dosage, alkaline solid waste ratio,
110 mineral ratio, and water-to-binder ratio were designed, comprising 18 specimens. Macroscopic properties were
111 evaluated by 3 d, 7 d, and 28 d compressive strength tests, combined with XRD, FTIR, and SEM-EDS analyses.
112 The study systematically reveals the coupled effects of variables on hydration products, microstructure, and
113 mechanical properties, clarifies the self-activation mechanism and microstructure-performance relationship, and
114 provides theoretical and technical support for optimization, engineering application, and low-carbon development
115 of high-performance all-solid-waste cementitious materials.

116 **2. Materials and methods**

117 **2.1. Raw materials and their properties**

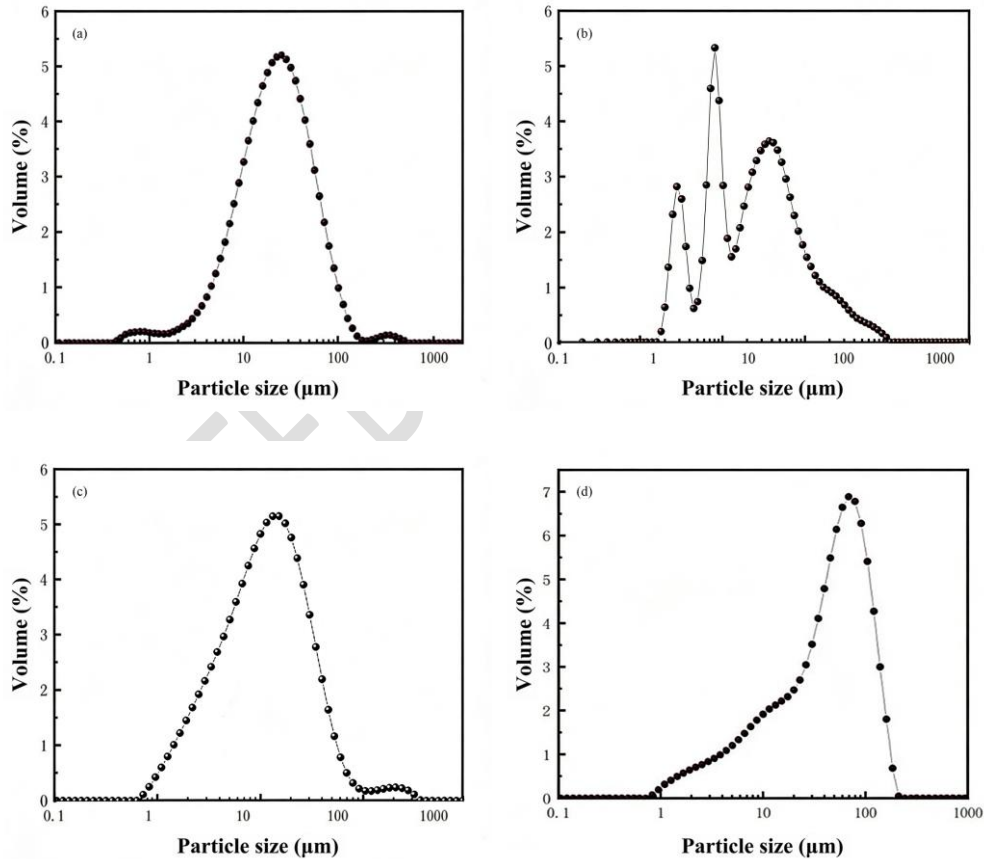
118 In this study, an all-solid-waste cementitious material was prepared with CS and NDA as alkaline solid activators,
 119 and GGBS and BA as main precursors. Raw material pretreatment: CS (off-white powder, Yangquan, Shanxi) was
 120 dried and ball-milled for 15 min for particle refinement; NDA (coal-fired power plant desulfurization byproduct)
 121 was only dried for moisture removal; S105-grade GGBS (Wuhan Iron and Steel Group, GB/T18046) was dried to
 122 constant weight at $100\pm 5^\circ\text{C}$; BA (Hebei metallurgical plant) was dried to constant weight at $100\pm 5^\circ\text{C}$, ball-milled
 123 for activation, and sieved to remove coarse particles.

124

Table 1 Physical properties of CS, NDA, GGBS and BA

Materials	Particle size parameters			Specific surface area/ $\text{m}^2\cdot\text{kg}^{-1}$
	D10/ μm	D50/ μm	D90/ μm	
CS	5.945	20.712	59.384	565
NDA	0.318	2.255	12.72	2207
GGBS	2.469	10.568	33.524	765.69
BA	5.487	43.466	104.093	447

125



126

127

Fig. 1 Particle size distribution of (a) CS, (b) NDA, (c) GGBS and (d) BA

128

129

130

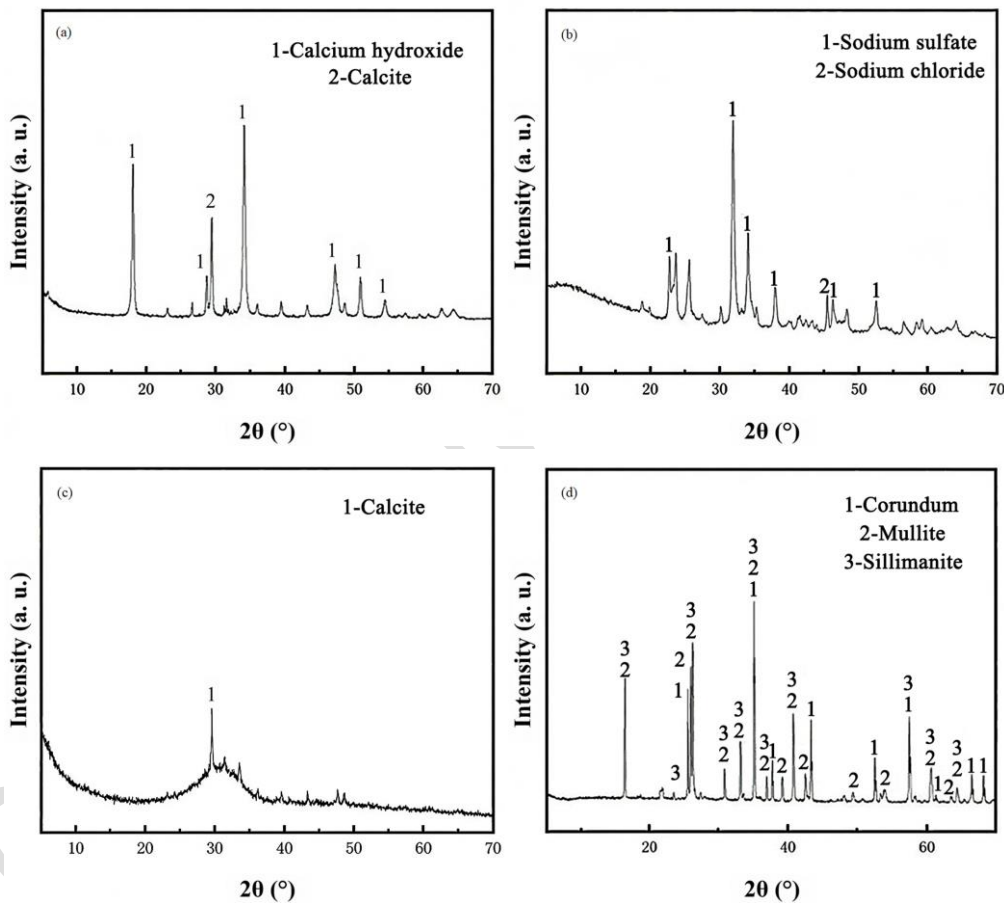
131

Prior to testing, all raw materials were dried to below 1% moisture content. CS and BA were further ground at 300 r/min for 15 min to optimize particle size distribution. A laser particle size analyzer (Malvern Mastersizer 2000, UK) and the BET method were then used to measure particle size distribution and specific surface area of the five raw materials, with results presented in **Table 1** and **Fig. 1**. Laser particle size analysis showed that the five raw materials

132 had PSDs ranging from 0.1 to 1000 μm , with D50 values of 20.712 μm for CS, 2.255 μm for NDA, 10.568 μm for
 133 GGBS, and 43.466 μm for BA. BET results indicated SSAs of 565 m^2/kg for CS, 765.69 m^2/kg for GGBS, and 447
 134 m^2/kg for BA, while NDA exhibited the highest SSA of 2207 m^2/kg .

135 **Table 2** Chemical composition and content of CS, NDA, GGBS and BA

Materials	Mass fraction of each component (%)											
	CaO	SiO ₂	Cl	Al ₂ O ₃	MgO	Na ₂ O	SO ₃	Fe ₂ O ₃	TiO ₂	MnO	K ₂ O	P ₂ O ₅
CS	94.737	2.415	-	1.228	-	-	0.779	0.518	0.089	-	-	-
NDA	0.47	0.67	3.30	0.55	0.08	47.91	46.62	0.18	0.05	-	0.07	-
GGBS	49.034	26.641	-	13.123	5.71	0.467	1.933	0.327	1.467	0.687	0.412	-
BA	0.562	21.049	-	69.234	0.181	-	0.092	1.997	6.279	-	0.189	0.218



137 **Fig. 2** The XRD patterns of raw materials: (a) CS, (b) NDA, (c) GGBS and (d) BA.

138 X-ray Diffraction (XRD) was used to characterize the chemical composition and mineral phase composition of the
 139 five raw materials, with detailed results shown in **Table 2** and **Fig. 2**. Analysis showed that CS is dominated by CaO
 140 at 94.737%, with calcium hydroxide and calcite as the main phases. NDA mainly contains Na₂O at 47.91% and SO₃
 141 at 46.62%, with sodium sulfate and sodium chloride as primary phases. GGBS is rich in CaO at 49.034% and SiO₂
 142 at 26.641%; its main crystalline phase is calcite, and a broad hump at 20°–40° indicates abundant reactive
 143 amorphous aluminosilicates. BA contains high Al₂O₃ at 69.234% and SiO₂ at 21.049%, with corundum, mullite, and
 144 sillimanite as major phases. All materials are rich in Ca, Si, and Al, among which Si and Al exhibit pozzolanic
 145

146 reactivity, providing a solid basis for CNGA hydration.

147 **2.2. Test specimen preparation**

148 The preparation of paste specimens for the all-solid-waste cementitious material includes three stages: raw material
149 pretreatment, paste preparation, and specimen molding and curing.

150 (1) Raw material pretreatment: Solid waste materials were dried in an electric thermostatic blast dryer at $105\pm 5^{\circ}\text{C}$
151 for 24 h to ensure moisture content below 1%. The dried materials were mechanically activated using a vertical
152 planetary ball mill (XQM-4), which reduced D50 and enhanced pozzolanic activity.

153 (2) Paste preparation: Raw materials were weighed according to the designed mix using an electronic balance with
154 0.01 g accuracy. Mixing water was controlled by pipette based on the preset water-to-binder ratio. A planetary mixer
155 (JJ-5) was used, with 10 s initial mixing, 120 s low-speed mixing, a 15 s rest, and 120 s high-speed mixing to obtain
156 a homogeneous paste.

157 (3) Specimen molding and curing: 40 mm cube molds were pre-coated with release agent. The paste was placed in
158 three layers and vibrated for 40 s per layer to remove air. After surface leveling, molds were sealed with plastic film
159 and cured at $20\pm 2^{\circ}\text{C}$ and relative humidity $\geq 95\%$ for 24 h. Specimens were then demolded and stored in the curing
160 room under constant conditions until the designated ages.

161 **2.3. Test methods**

162 **2.3.1 Compressive strength test**

163 Paste specimens in this study were tested with adjusted molding parameters with reference to 'Test Method for
164 Strength of Cement Mortar (ISO Method)'(GB/T17671-2021)[33]. Paste samples cured under standard conditions
165 for 3d, 7d, and 28d were subjected to compressive strength testing.

166 **2.3.2 X-ray diffraction (XRD)**

167 The phase composition of raw materials and hydration products was analyzed using a Rigaku D/max-2550 X-ray
168 diffractometer. The operating voltage and current were set to 40 kV and 150 mA, respectively, with Cu K α radiation
169 as the X-ray source. The scanning range was 5° - 70° 2θ at a scanning speed of $5^{\circ}/\text{min}$. Jade-6 software was used for
170 the analysis of XRD patterns.

171 **2.3.3 Fourier transform infrared spectroscopy (FTIR)**

172 Fourier transform infrared spectroscopy (FTIR) analysis of hydration product powders was performed using a
173 Nicolet is 10; Nexus 670 spectrometer. The test was conducted in absorbance mode with a wavenumber range of
174 $400\text{--}4000\text{ cm}^{-1}$.

175 **2.3.4 Scanning electron microscopy-energy dispersive spectroscopy (SEM-EDS)**

176 A ZEISS Gemini 300 scanning electron microscope was used to examine the morphology and micro-area
177 composition of hardened paste. Specimens cured to the target age were sampled from the middle, and the fragments
178 were ground and polished into smooth thin sections for analysis of hydration product morphology and composition.

179 **2.4. Experimental scheme**

180 This study developed an all-solid-waste cementitious material using CS and NDA as alkaline activators and GGBS
 181 and BA as precursors. A composite system was designed by varying NDA content, alkaline solid waste proportion,
 182 mineral ratio, and water-to-binder ratio. XRD and FTIR were used to identify hydration product types and contents,
 183 while SEM-EDS analyzed microstructure and hydration behavior, to clarify the coupled effects of these parameters
 184 on material properties and microstructure. The variable levels for each group are detailed in Table 3:

185 **Table 3** CNGA system mix ratio design

Series	NO.	NDA/%	CS/%	GGBS/%	BA/%	Water-to-binder ratio
Group A: NDA content	CNGA-1	0	40	40	20	0.45
	CNGA-2	2	38	40	20	0.45
	CNGA-3	4	36	40	20	0.45
	CNGA-4	6	34	40	20	0.45
Group B: Alkaline solid waste mix ratio	CNGA-5	0	50	30	20	0.45
	CNGA-6	0	45	35	20	0.45
	CNGA-7	0	35	45	20	0.45
	CNGA-8	0	30	50	20	0.45
Group C: Mineral mix ratio(4%NDA)	CNGA-9	4	36	60	0	0.45
	CNGA-10	4	36	50	10	0.45
	CNGA-3	4	36	40	20	0.45
	CNGA-11	4	36	30	30	0.45
Group C: Mineral mix ratio(0%NDA)	CNGA-12	0	40	60	0	0.45
	CNGA-13	0	40	50	10	0.45
	CNGA-14	0	40	40	20	0.45
	CNGA-15	0	40	30	30	0.45
Group D: Water-to-binder ratio	CNGA-16	4	36	40	20	0.39
	CNGA-17	4	36	40	20	0.42
	CNGA-3	4	36	40	20	0.45
	CNGA-18	4	36	40	20	0.48

186 **3. Results and discussion**

187 **3.1. Macro-performance results and analysis**

188 3.1.1 Analysis of the effect of NDA content

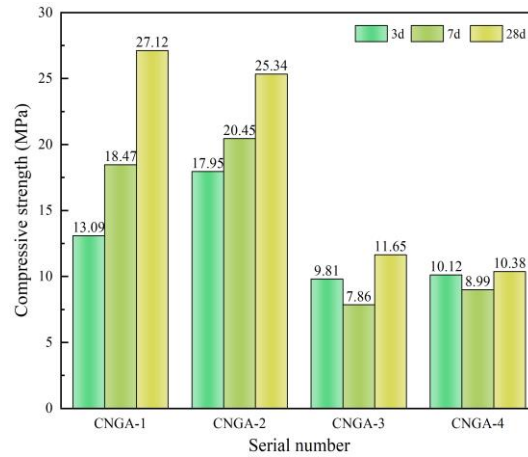


Fig. 3 Effect of different NDA contents on the mechanical properties of the CNGA system

Table 4 Effect of different NDA contents on the mechanical properties of the CNGA system

NO.	NDA Content/%	Compressive strength/MPa		
		3d	7d	28d
CNGA-1	0	13.09	18.47	27.12
CNGA-2	2	17.95	20.45	25.34
CNGA-3	4	9.81	7.86	11.65
CNGA-4	6	10.12	8.99	10.38

189
190
191

192 In this subsection, the NDA content was selected as the primary variable (0%, 2%, 4%, and 6%), with the CS content
193 synchronously adjusted from 40% to 34%. The contents of GGBS (40%) and BA (20%), as well as the water-to-
194 binder ratio (0.45), were kept constant to investigate their effects on the 3-, 7-, and 28-day compressive strengths of
195 the CNGA all-solid-waste cementitious material. The experimental data were presented in **Table 4** and **Fig. 3**.

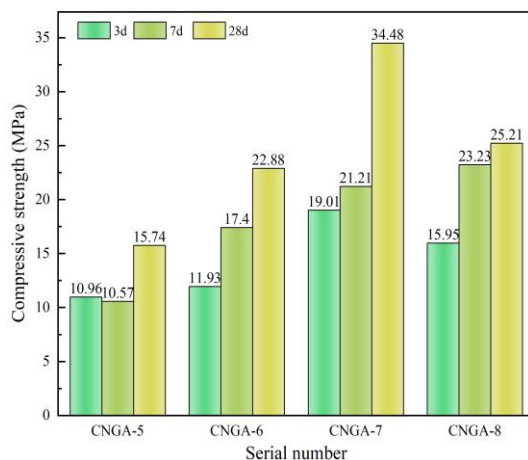
196 The incorporation of NDA enhanced the early-age reactivity of GGBS and BA. Alkaline components released from
197 NDA accelerated hydration, promoted product formation, and densified the internal structure, improving early-age
198 performance. For CNGA1 with 0% NDA, the 3 d, 7 d, and 28 d compressive strengths were 13.09 MPa, 18.47 MPa,
199 and 27.12 MPa, respectively, showing stable strength development and reflecting the baseline performance without
200 sodium-based activators.

201 In the CNGA-2 sample containing 2% NDA, the 3d compressive strength increased to 17.95 MPa (a 37%
202 improvement compared to CNGA-1), and the 7d strength reached 20.45 MPa, indicating a significant enhancement
203 in early-age strength. However, the 28d strength slightly decreased to 25.34 MPa. The alkaline components released
204 by the appropriate amount of NDA accelerated the early hydration of GGBS and BA, forming a dense structure.
205 Nevertheless, minor side reactions consumed partial reactive components in the later stage, leading to a slight
206 strength retrogression.

207 When the NDA content exceeded 2%, the compressive strength of the CNGA system decreased markedly. Excessive
208 NDA induced an over-alkaline environment, which suppressed effective activation of GGBS and BA and reduced
209 the formation of C-S-H gel. Meanwhile, intensified side reactions increased internal porosity and deteriorated matrix
210 compactness, ultimately leading to significant strength loss.

211 Overall, the CNGA system exhibited optimal compressive strength at an NDA content of 2%, while further increases
 212 in NDA dosage led to significant strength reduction due to excessive alkalinity and inhibited hydration.

213 3.1.2 Analysis of the effect of alkaline solid waste mix ratio



214 **Fig. 4** Effect of alkaline solid waste mix ratio on compressive strength of CNGA system

215 **Table 5** Effect of alkaline solid waste mix ratio on compressive strength of CNGA system

216

NO.	CS/%	GGBS/%	Compressive strength/MPa		
			3d	7d	28d
CNGA-5	50	30	10.96	10.57	15.74
CNGA-6	45	35	11.93	17.40	22.88
CNGA-7	35	45	19.01	21.21	34.48
CNGA-8	30	50	15.95	23.23	25.21

217 For this experimental group, the NDA content was fixed at 0%, the BA content at 20%, and the water-to-binder ratio
 218 at 0.45. By adjusting the proportion of CS to GGBS (with CS decreasing from 50% to 30% and GGBS increasing
 219 synchronously from 30% to 50%), the synergistic effect of alkaline solid wastes and precursors on the strength of
 220 the CNGA all-solid-waste cementitious material was investigated. The experimental data were presented in **Table**
 221 **5** and **Fig. 4**.

222 The compressive strengths of CNGA-5 at 3, 7, and 28 d were 10.96 MPa, 10.57 MPa, and 15.74 MPa, respectively.
 223 Its strength was lower than other mixtures: despite sufficient alkalinity from the high CS content, insufficient GGBS
 224 limited the supply of reactive components, resulting in inadequate hydration and restrained strength development.

225 For CNGA-6 (CS reduced to 45%, GGBS increased to 35%), the 3, 7, and 28 d strengths reached 11.93 MPa, 17.40
 226 MPa, and 22.88 MPa, respectively, with a significant strength increase. The results indicate that the higher GGBS
 227 proportion facilitated the formation of hydration products and enhanced the material's compactness.

228 CNGA-7 (CS further reduced to 35%, GGBS increased to 45%) achieved the optimal mechanical properties, with
 229 3, 7, and 28 d strengths of 19.01 MPa, 21.21 MPa, and a peak value of 34.48 MPa, respectively. At this ratio, the
 230 alkalinity from CS and reactive components in GGBS reached an optimal balance: sufficient reactive ingredients
 231 generated abundant C-S-H gel to fill pores, markedly enhancing matrix density and mechanical strength.

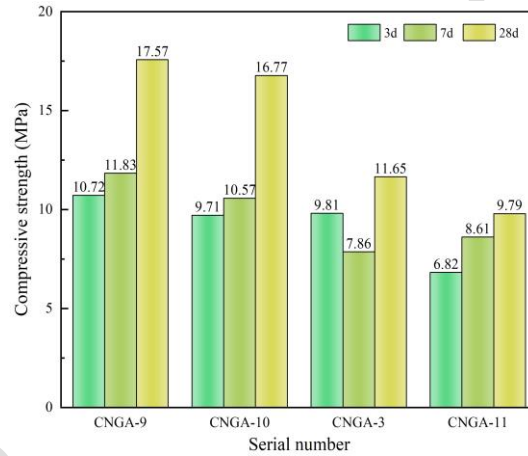
232 For CNGA-8 (CS decreased to 30%, GGBS increased to 50%), the 3 and 7 d strengths were 15.95 MPa and 23.23
 233 MPa, respectively, but the 28 d strength dropped to 25.21 MPa. Excessively low CS content led to insufficient

234 system alkalinity, causing incomplete GGBS hydration and restricted late-age strength development.
 235 Overall, the CS-to-GGBS ratio exerted a significant influence on the mechanical properties of the CNGA system.
 236 The CNGA-7 sample, with 35% CS and 45% GGBS, exhibited the best performance. Excessively high CS content
 237 increased porosity and reduced compactness, whereas insufficient CS failed to provide adequate alkalinity to fully
 238 activate GGBS, ultimately leading to reduced strength.

239 3.1.3 Analysis of the effect of BA content

240 This experimental group investigated the effect of BA content on the compressive strength of CNGA all-solid-waste
 241 cementitious material under two scenarios: with and without NDA addition, while analyzed the mechanism of action
 242 of BA on the all-solid-waste cementitious material under each scenario. The influence of BA content on the
 243 compressive strength of CNGA all-solid-waste cementitious material with NDA addition was presented in **Table 6**
 244 and **Fig. 5**, while that without NDA addition was shown in **Table 7** and **Fig. 6**.

245 (1) Effect of BA content under 4% NDA addition



246 **Fig. 5** Effect of BA content on compressive strength of CNGA under 4% NDA addition

247 **Table 6** Effect of BA content on compressive strength of CNGA under 4% NDA addition

248

NO.	NDA Content/%	BA Content/%	Compressive strength/MPa		
			3d	7d	28d
CNGA-9	4	0	10.72	11.83	17.57
CNGA-10	4	10	9.71	10.57	16.77
CNGA-3	4	20	9.81	7.86	11.65
CNGA-11	4	30	6.82	8.61	9.79

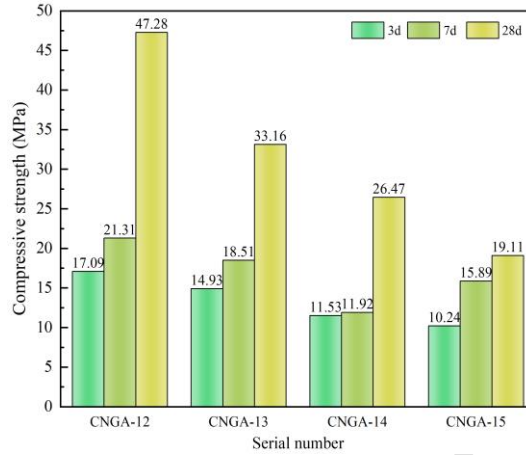
249 For the CNGA-9 sample with 0% BA content, the 3-day, 7-day, and 28-day compressive strengths were 10.72 MPa,
 250 11.83 MPa, and 17.57 MPa, respectively, exhibiting stable strength development. In the absence of BA, the all-
 251 solid-waste cementitious material underwent uniform hydration reactions.

252 With the BA content increased to 10%, the 3d strength slightly decreased to 9.71 MPa, while the 7d and 28d strengths
 253 were 10.57 MPa and 16.77 MPa, respectively. These results suggest that a low BA content had no significant
 254 influence on the compressive strength of the CNGA system.

255 Elevated BA content significantly degraded the mechanical properties of the CNGA material: 20% BA caused a

256 sharp strength drop (3 d: 9.81 MPa, 7 d: 7.86 MPa, 28 d: 11.65 MPa), which further declined at 30% BA (3 d: 6.82
 257 MPa, 28 d: 9.79 MPa). This stems from uneven reaction between excess BA and NDA, which triggers imbalanced
 258 hydration product distribution and higher porosity.

259 (2) Effect of BA content under 0% NDA addition



260 **Fig. 6** Effect of BA content on compressive strength of CNGA under 0% NDA addition

261 **Table 7** Effect of BA content on compressive strength of CNGA under 0% NDA addition

262

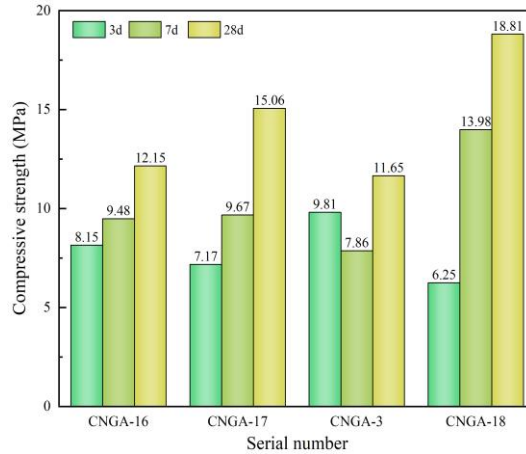
NO.	BA Content/%	Compressive strength/MPa		
		3d	7d	28d
CNGA-12	0	17.09	21.31	47.28
CNGA-13	10	14.93	18.51	33.16
CNGA-14	20	11.53	11.92	26.47
CNGA-15	30	10.24	15.89	19.11

263 Without NDA addition, the effect of BA content on the compressive strength of the CNGA all-solid-waste
 264 cementitious material showed a distinct pattern compared with the 4% NDA group. CNGA-12 (0% BA) achieved
 265 the highest overall strength, with 3 d, 7 d, and 28 d compressive strengths of 17.09 MPa, 21.31 MPa, and 47.28
 266 MPa, respectively. This indicates that the CNGA system underwent more complete hydration without NDA and BA,
 267 where hydration products filled internal pores to form a denser matrix structure.

268 Increasing BA content led to continuous strength degradation: 10% BA gave a 3 d strength of 14.93 MPa and 28 d
 269 strength of 33.16 MPa (stable but inferior to CNGA-12), which further dropped to 11.53 MPa (3 d) and 26.47 MPa
 270 (28 d) at 20% BA, and plummeted to 19.11 MPa at 28 d for 30% BA (a 51% reduction vs. CNGA-12). This severe
 271 strength attenuation stems from excessive BA, which cannot participate in effective hydration, increases internal
 272 porosity, and inhibits hydration product formation.

273 Overall, increasing BA content generally exerted a negative effect on the compressive strength of the CNGA system,
 274 and this effect was strongly dependent on NDA content. Under 4% NDA addition, excessive BA significantly
 275 reduced strength, particularly at BA contents of 20% or higher. In contrast, the system without both BA and NDA
 276 achieved the highest strength. These results indicate that BA exhibits relatively low reactivity, and excessive BA
 277 primarily increases porosity rather than contributing to effective hydration.

278 3.1.4 Analysis of the effect of water-to-binder ratio



279 **Fig. 7** Effect of water-to-binder ratio on the compressive strength of CNGA system

280 **Table 8** Effect of water-to-binder ratio on compressive strength of CNGA system

281

NO.	Water-to-binder ratio	Compressive strength/MPa		
		3d	7d	28d
CNGA-16	0.39	8.15	9.48	12.15
CNGA-17	0.42	7.17	9.67	15.06
CNGA-3	0.45	9.81	7.86	11.65
CNGA-18	0.48	6.25	13.98	18.81

282 For this experimental group, the NDA content (4%), CS proportion (36%), GGBS proportion (40%), and BA content
 283 (20%) were fixed, and a gradient of water-to-binder ratios (0.39, 0.42, 0.45, 0.48) was set for samples CNGA-16 to
 284 CNGA-18 and CNGA-3. The aim was to investigate the effect of varying water-to-binder ratios on the compressive
 285 strength of CNGA all-solid-waste cementitious material. The influence of the water-to-binder ratio on compressive
 286 strength was presented in **Table 8** and Fig. 7.

287 For CNGA-16 with a water-to-binder ratio of 0.39, the early-age compressive strengths were relatively high (3 d:
 288 8.15 MPa, 7 d: 9.48 MPa), while the 28 d strength was limited to 12.15 MPa. Although the low water-to-binder ratio
 289 reduces free water content and enables the all-solid-waste cementitious material to form a relatively dense structure
 290 in the early stage, insufficient moisture restricts late-age hydration reactions. Reactive components such as GGBS
 291 and BA cannot be fully dissolved and reacted, resulting in inadequate C-S-H gel formation and slow late-age
 292 strength gain.

293 When the water-to-binder ratio was increased to 0.42 (CNGA-17), the 3d strength decreased to 7.17 MPa (a 12.0%
 294 decrease compared to CNGA-16), but the 28d strength increased to 15.06 MPa (a 23.9% increase). A moderate
 295 increase in water content improved paste fluidity, facilitating more thorough diffusion of reactants (Ca^{2+} , SiO_2 , and
 296 Al_2O_3) and more complete late-age hydration. The increased formation of C-S-H gel and AFt offsets the loss of
 297 early-age strength.

298 CNGA3 with a water-to-binder ratio of 0.45 exhibited the lowest strength, with a 28 d compressive strength of 11.65
 299 MPa, 22.6% lower than CNGA17. This ratio led to an imbalance between water and reactive components.

300 Insufficient early hydration limited C–S–H formation and prevented development of a dense microstructure.
301 Although moisture remained at later stages, the lack of early reaction left few reactive components available,
302 restricting formation of sufficient cementitious products for pore filling and resulting in reduced macroscopic
303 strength.

304 CNGA-18 (water-to-binder ratio 0.48) delivered the group's best long-term mechanical performance, with a 28 d
305 compressive strength of 18.81 MPa (54.8% higher than CNGA-16 at 0.39 water-to-binder ratio). The high water-
306 to-binder ratio sustains late-age hydration: ample moisture enables full dissolution of reactive components in GGBS
307 and BA, forming abundant C-S-H gel and AFt to densify the matrix. Despite a low 3 d strength of 6.25 MPa, the
308 sample achieved significant late-age strength growth.

309 The water-to-binder ratio had a nonlinear effect on the CNGA system's mechanical properties. The 0.39 ratio
310 benefited early strength but limited late hydration, the 0.48 ratio ensured sufficient moisture for sustained hydration
311 and optimal late-age strength, while the 0.45 ratio performed worst due to water-reactive component imbalance.
312 Thus, 0.48 was identified as the system's optimal water-to-binder ratio.

313 **3.2. Microscopic analysis of hydration products**

314 3.2.1 XRD analysis of hydration products

315 As illustrated in Fig. 8, multiple reaction products were identified in the CNGA1–3 samples, including calcium
316 silicate hydrate (C–S–H), portlandite ($\text{Ca}(\text{OH})_2$), calcite, hydrocalumite, AFt, gypsum, and a small amount of mullite.
317 NDA enhances the alkaline environment by releasing Na^+ . An appropriate dosage promotes GGBS hydration and
318 accelerates C–S–H formation, improving strength. However, excessive NDA creates an overly alkaline environment
319 that suppresses effective C–S–H formation and promotes non-dominant phases such as calcite and hydrocalumite,
320 reducing strength. As the main calcium source, CS supplies Ca^{2+} and OH^- to activate GGBS and BA. Hydration of
321 CaO in CS produces substantial $\text{Ca}(\text{OH})_2$, which maintains alkalinity and participates in C–S–H formation.
322 GGBS is the primary strength contributor in the all-solid-waste cementitious material. Under alkaline conditions,
323 CaO and SiO_2 in GGBS hydrate to form C–S–H gel with an acicular fibrous structure, enhancing matrix
324 compactness and mechanical properties. In CNGA3, this phase evolution aligns with the strength degradation
325 mechanism in Section 3.1.1, where excessive NDA inhibits effective C–S–H formation. By supplying Al_2O_3 , BA
326 reacts with Ca^{2+} under alkaline conditions to form hydrocalumite and AFt. An appropriate BA content promotes the
327 formation of C–A–H and hydrocalumite, improving early-age strength and chemical stability.

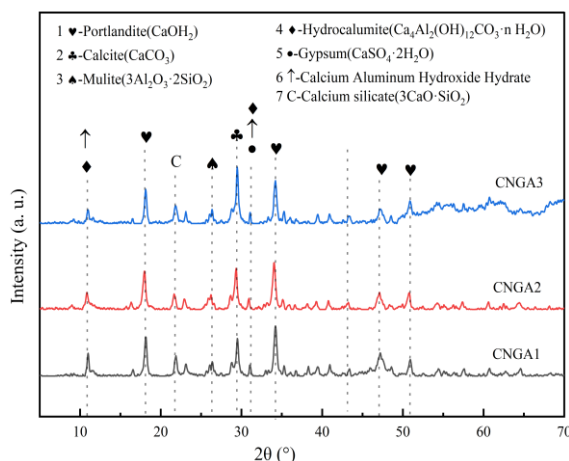


Fig. 8 XRD patterns of CNGA1-3 system

328
329
330
331

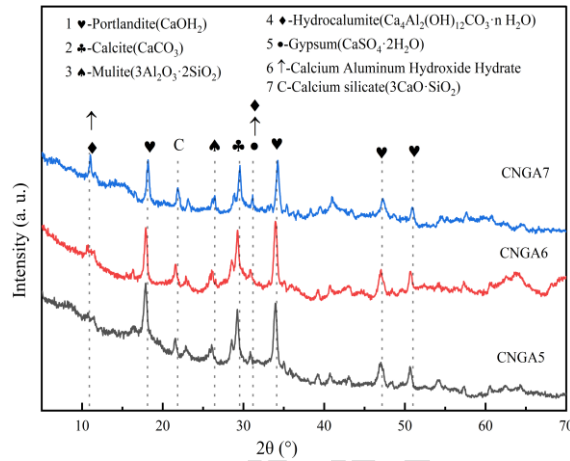
Table 9 XRD analysis of hydration products in the CNGA system with different sodium-based desulfurization ash contents

Characteristic peaks ($^{\circ}2\theta$)	Hydration products	Relationship with performance
18 $^{\circ}$ and 41 $^{\circ}$	Ca(OH) ₂	While Ca(OH) ₂ contributes little directly to strength, the alkaline environment it provides promotes GGBS activation. However, excessive Ca(OH) ₂ may impair matrix performance by forming calcite through carbonation.
18 $^{\circ}$, 25 $^{\circ}$ and 32 $^{\circ}$	C-S-H	The higher the C-S-H content, the stronger the matrix cohesion and compactness—making it the primary contributor to the strength of the all-solid-waste cementitious material.
29 $^{\circ}$ and 50 $^{\circ}$	Calcite	An appropriate amount of Calcite fills internal pores and enhances chemical stability, while excess Calcite increases porosity and weakens mechanical strength.
9.1 $^{\circ}$, 15.7 $^{\circ}$, 18.8 $^{\circ}$, 22.9 $^{\circ}$ and 25.6 $^{\circ}$	AFt	The formation of AFt contributes to early-age strength development, but excessive AFt may induce expansive cracks in the matrix.
11.6 $^{\circ}$, 20.7 $^{\circ}$, 29.2 $^{\circ}$ and 31.1 $^{\circ}$	Gypsum	Gypsum is a non-cementitious phase; excessive Gypsum content may lead to increased porosity of the material.
11 $^{\circ}$ and 31 $^{\circ}$	Hydrocalumite	The flaky structure of Hydrocalumite contributes minimally to strength but enhances the chemical stability of the material.
16 $^{\circ}$ and 33 $^{\circ}$	Mullite	Mullite exhibits high chemical stability but is a non-cementitious phase, providing limited contribution to the material's strength.

332 Based on **Table 9** and **Fig. 8**, CNGA1 (0% NDA) is dominated by C-S-H (characteristic peaks at 18 $^{\circ}$, 25 $^{\circ}$, 32 $^{\circ}$) and
 333 Ca(OH)₂ (characteristic peaks at 18 $^{\circ}$, 41 $^{\circ}$). A small amount of unreacted phases remains in the system. As the core
 334 cementitious phase, C-S-H forms a dense fibrous network, which is consistent with the macroscopic performance
 335 of a 28-day compressive strength of 27.12 MPa. Ca(OH)₂ provides a stable alkaline environment, with no
 336 pronounced carbonation detected.

337 In the CNGA2 (2% NDA) sample, C-S-H and $\text{Ca}(\text{OH})_2$ remain the main products, accompanied by a moderate
338 formation of Calcite (characteristic peaks at 29° , 50°), which reflects good compactness. Its 28-day strength (25.34
339 MPa) is only slightly lower than that of CNGA1.

340 In CNGA3 with 4% NDA, product composition changes markedly. Calcite and hydrocalumite increase significantly,
341 with characteristic peaks at 11° and 31° , while C-S-H decreases sharply. At the same time, AFt with peaks at 9.1°
342 and 15.7° and gypsum with peaks at 11.6° and 20.7° are enhanced. Non-cementitious phases such as calcite and
343 gypsum become dominant, weakening cohesion and compactness and leading to a sharp reduction in 28 d strength
344 to 11.65 MPa.



345
346 **Fig. 9** XRD patterns of CNGA5-7 system

347 XRD patterns of CNGA5-7 samples are displayed in **Fig. 9**. For CNGA5 (50% CS, 30% GGBS), the characteristic
348 peaks of $\text{Ca}(\text{OH})_2$ (18° , 41°) are the strongest, while those of C-S-H (18° , 25° , 32°) are relatively weak. As indicated
349 by the intense peaks at 18° , 25° , and 32° in the XRD patterns, although the high $\text{Ca}(\text{OH})_2$ content in CNGA5
350 provides a relatively strong alkaline environment, the insufficient proportion of GGBS restricts the formation of C-
351 S-H. The flaky structure of $\text{Ca}(\text{OH})_2$ can offer an alkaline environment for activating GGBS, but it contributes little
352 to strength itself. Additionally, the limited formation of calcite suggests a reduced pore-filling effect, leading to a
353 28d strength of only 15.74 MPa.

354 In the CNGA6 sample (45% CS, 35% GGBS), the formation of C-S-H increases, and an appropriate amount of
355 Calcite fills part of the pores. A characteristic peak of Hydrocalumite at 11° emerges, indicating that BA undergoes
356 hydration to form Hydrocalumite under alkaline conditions. Despite its limited contribution to strength, this flaky
357 Hydrocalumite plays a crucial role in enhancing the material's chemical stability. The increased GGBS proportion
358 facilitates the formation of a C-S-H gel network, and Calcite fills partial pores, resulting in an improved 28d strength
359 of 22.88 MPa.

360 For CNGA7 (35% CS, 45% GGBS), C-S-H formation is maximized, and its fibrous structure forms a dense matrix
361 network. Calcite peak intensity increases, indicating more calcite from $\text{Ca}(\text{OH})_2$ carbonation contributes to pore
362 filling. Hydrocalumite and gypsum peaks are also more pronounced, reflecting byproducts of BA reactions under
363 CS activation. These phases assist pore filling and early strength, though excessive amounts may cause

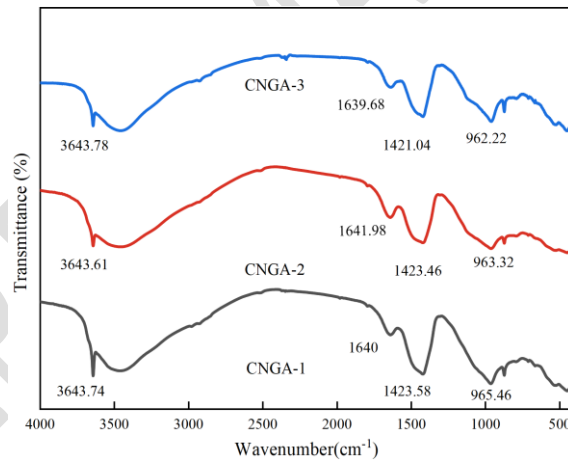
364 microcracking or increased porosity. CNGA7 exhibits the densest microstructure and achieves a 28 d strength of
365 34.48 MPa, the highest among the three materials.

366 Overall, C-S-H is the primary cementitious phase controlling CNGA strength. Its formation is enhanced by higher
367 GGBS content and appropriate NDA dosage, improving mechanical performance. $\text{Ca}(\text{OH})_2$ mainly provides
368 alkalinity, but excess $\text{Ca}(\text{OH})_2$ readily carbonates to calcite, potentially reducing strength. Moderate calcite aids
369 pore filling and stability, whereas excess weakens the matrix. Increasing GGBS is key to strength enhancement, as
370 evidenced by CNGA7 achieving the highest compressive strength.

371 3.2.2 FTIR analysis of hydration products

372 FTIR spectra of CNGA1-3 samples are presented in **Fig. 10**, and the corresponding absorption peak assignments
373 were summarized in **Table 10**. The absorption peak at 3640 cm^{-1} in the FTIR spectra corresponds to the O-H
374 stretching vibration of $\text{Ca}(\text{OH})_2$, originating from the hydration of CaO in CS ($\text{CaO} + \text{H}_2\text{O} \rightarrow \text{Ca}(\text{OH})_2$). This peak
375 can be regarded as an indicator of the alkaline environment favorable for C-S-H formation.

376 CNGA1 shows the strongest $\text{Ca}(\text{OH})_2$ absorption peak, indicating higher content that maintains alkalinity for GGBS
377 hydration. With increasing NDA dosage, $\text{Ca}(\text{OH})_2$ in CNGA2 and CNGA3 progressively carbonates to calcite,
378 causing a gradual decrease of the 3640 cm^{-1} peak, while calcite peaks at 1420 cm^{-1} and 874 cm^{-1} become more
379 pronounced. In CNGA2, moderate calcite aids pore filling and improves stability, whereas excessive calcite in
380 CNGA3 increases porosity and reduces mechanical strength.



381
382 **Fig. 10** FTIR patterns of sodium group content of CNGA1-3 system

383 Absorption peaks at $3400\text{--}3200\text{ cm}^{-1}$ and $1600\text{--}1680\text{ cm}^{-1}$ correspond to bound water in hydration products, mainly
384 associated with C-S-H gel, and their intensity reflects the degree of hydration. CNGA3 shows relatively strong
385 bound-water peaks under high NDA dosage, indicating an intensified hydration environment. However, the
386 increased bound water did not fully transform into C-S-H; instead, higher amounts of byproducts such as calcite
387 and gypsum adversely affected the strength of the all-solid-waste cementitious material.

388 In the $1100\text{--}950\text{ cm}^{-1}$ range, Si-O-Si stretching peaks characteristic of C-S-H indicate the main cementitious phase
389 governing cohesion and compactness. CNGA1 shows the strongest Si-O-Si peak, implying higher C-S-H content
390 and a 28 d strength of 27.12 MPa. CNGA2 has slightly lower C-S-H, but moderate calcite formation aids pore

391 filling, yielding a 28 d strength of 25.34 MPa, close to CNGA1. In CNGA3, C–S–H decreases markedly with the
 392 weakest peak intensity; enhanced carbonate- and sulfate-related peaks indicate increased calcite and gypsum,
 393 corresponding to reduced C–S–H and weakened mechanical performance.

394 Gypsum peaks at 600–700 cm^{-1} originate from SO_4^{2-} bending vibrations. CNGA1 contains negligible gypsum. In
 395 CNGA2, limited gypsum may aid microstructural densification and early strength. In CNGA3, gypsum increases
 396 markedly, likely due to SO_4^{2-} combining with Ca^{2+} at high NDA dosage. As a non-cementitious phase, excess
 397 gypsum increases porosity and may reduce long-term strength.

398 **Table 10** FTIR absorption peaks for CNGA system

Wavenumber (cm^{-1})	Corresponding functional groups	Main sources	Relationship with performance
3640	O-H stretching vibration	$\text{Ca}(\text{OH})_2$	Provides an alkaline environment, promotes C-S-H formation, and enhances material strength.
1640,3400	H-O-H bending vibration	Bound water in hydration products	Reduced bound water decreases the content of hydration products in the all-solid-waste cementitious material and impairs strength.
1420,874	CO_3^{2-} stretching and bending vibrations	Calcite(CaCO_3)	As a non-cementitious phase, Calcite inhibits C-S-H formation, increases porosity, and reduces material strength.
960–1000	Si-O-Si stretching vibration	C-S-H, silicates	C-S-H is the primary strength-contributing phase, and a decrease in its content directly impairs the material's performance.
600–700	SO_4^{2-} bending vibration	Gypsum	Gypsum is a byproduct of side reactions that cannot enhance strength and may cause matrix deterioration.

399 The FTIR spectra of CNGA5–7 samples were shown in Fig. 11. The O–H stretching peak at $\sim 3640 \text{ cm}^{-1}$ corresponds
 400 to $\text{Ca}(\text{OH})_2$. CNGA5 shows the strongest $\text{Ca}(\text{OH})_2$ peak, indicating higher content consistent with its higher CS
 401 proportion. While CS supplies abundant Ca^{2+} and OH^- , excess $\text{Ca}(\text{OH})_2$ may inhibit effective C–S–H formation.
 402 Accordingly, the Si–O–Si band at 1100–950 cm^{-1} (C–S–H) is relatively weak in the FTIR spectra, indicating reduced
 403 C–S–H formation and a 28 d compressive strength of 15.74 MPa.

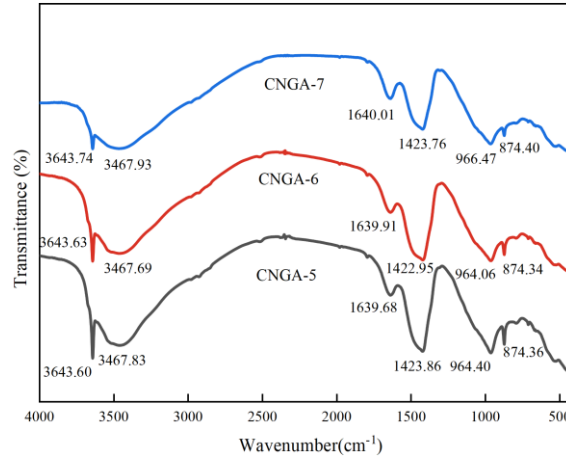


Fig. 11 FTIR profile of CNGA5-7 system

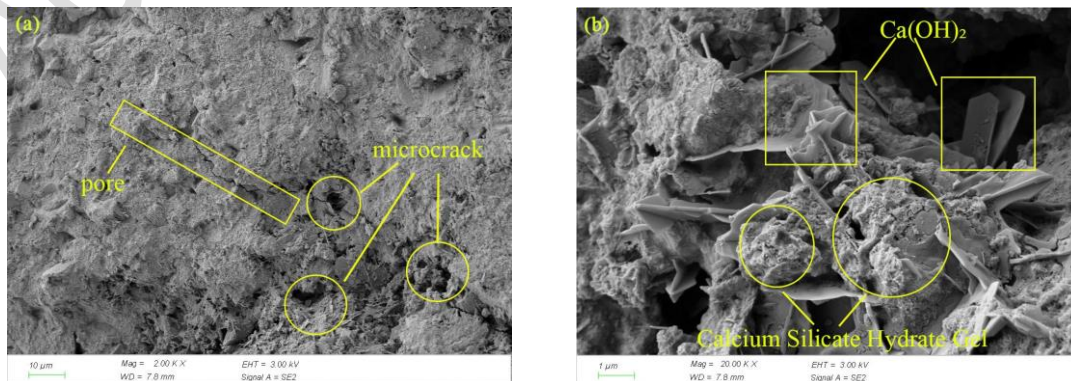
404
405

406 With increasing GGBS content, bound-water bands at $3400\text{--}3200\text{ cm}^{-1}$ intensify in CNGA6 and CNGA7, indicating
407 enhanced hydration. Calcite (CaCO_3) peaks at ~ 1410 and 874 cm^{-1} also strengthen, reflecting increased carbonation.
408 In CNGA6, moderate calcite has limited impact on strength, while the enhanced C–S–H peak at $1000\text{--}960\text{ cm}^{-1}$
409 indicates that a 35% GGBS proportion promotes C–S–H gel network formation, yielding a strength of 22.88 MPa.
410 In CNGA7, where the GGBS proportion is further increased to 45%, the FTIR patterns exhibit the most pronounced
411 absorption bands associated with Si–O–Si stretching vibration and bound water, indicating a relatively higher degree
412 of C–S–H formation at this ratio. Although the Calcite absorption peak intensifies further (indicating enhanced
413 carbonation), C–S–H remains the dominant phase, forming a dense network structure within the all-solid-waste
414 cementitious material. Consequently, the 28d strength reaches a maximum of 34.48 MPa.

415 $\text{Ca}(\text{OH})_2$ produced by CS hydration provides the alkaline environment required for GGBS activation, but excess
416 $\text{Ca}(\text{OH})_2$, as in CNGA5, readily carbonates to calcite. As the primary cementitious phase, C–S–H formation,
417 reflected by the Si–O–Si stretching intensity in FTIR spectra, governs CNGA strength. A moderate amount of calcite,
418 as in CNGA2, can fill micropores, whereas excessive calcite, as in CNGA3, hinders C–S–H interweaving and
419 degrades the microstructure and mechanical properties.

420 3.2.3 SEM analysis of hydration products

421 **Fig. 12** presents the microscopic morphology of the CNGA1 specimen (with 0% NDA and a 28-day compressive
422 strength of 27.12 MPa) after 28 days of hydration.



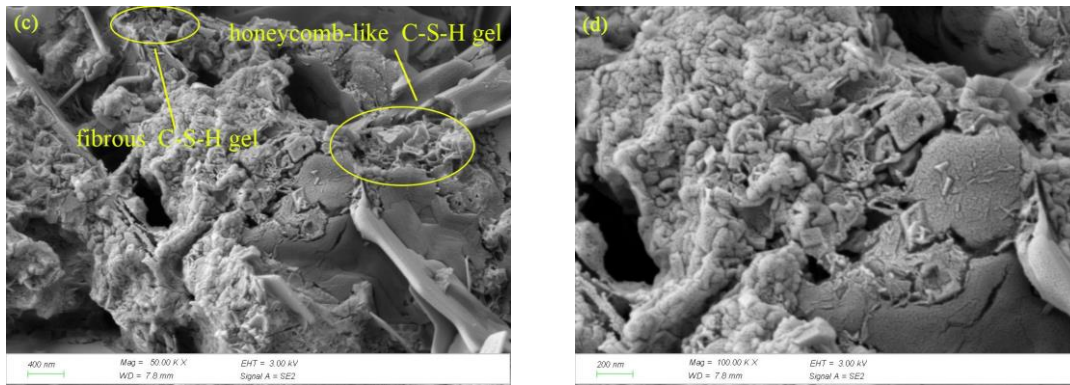
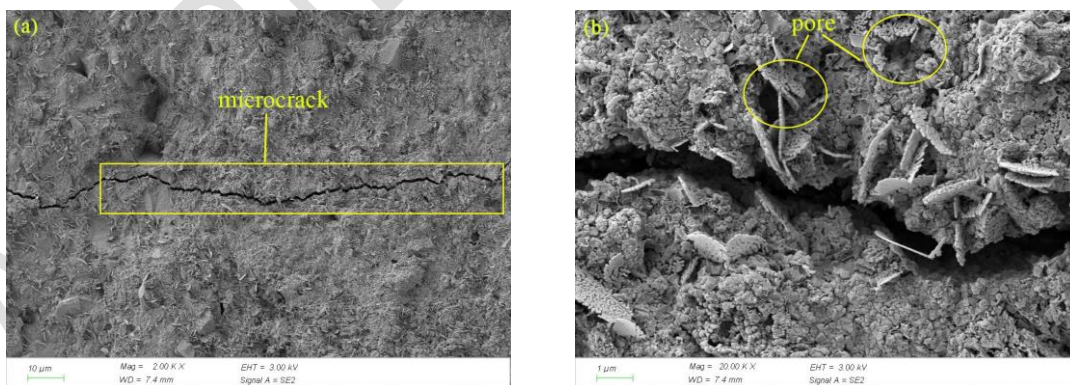


Fig. 12 Scanning electron micrograph of CNGA1 specimen 28d

423 As observed in Fig. 12, the CNGA1 specimen is relatively dense with low porosity, contributing to improved
 424 macroscopic mechanical properties. SEM images show flaky $\text{Ca}(\text{OH})_2$ and fibrous C-S-H. $\text{Ca}(\text{OH})_2$ presents a
 425 regular crystalline morphology and mainly provides an alkaline environment, while fibrous C-S-H forms a
 426 continuous network that governs strength. A small amount of unreacted GGBS particles is embedded in the gel
 427 matrix with negligible contribution to strength. C-S-H exhibits a typical fibrous or honeycomb-like structure,
 428 enhancing matrix bonding. Mineral crystals are tightly bonded without obvious large pores or cracks, indicating a
 429 high degree of hydration and uniform reaction in the all-solid-waste cementitious material.

430 Fibrous C-S-H gel is widely distributed and intertwined to form a dense network, providing the primary strength
 431 support for CNGA1, consistent with its 28 d compressive strength of 27.12 MPa. $\text{Ca}(\text{OH})_2$ crystals are regular and
 432 well dispersed, maintaining a stable alkaline environment that promotes C-S-H formation. A small amount of
 433 unhydrated particles is likely due to uneven distribution or locally insufficient alkalinity. Although they have little
 434 effect on current strength, they may gradually hydrate at later ages, further enhancing the strength of the all-solid-
 435 waste cementitious material.



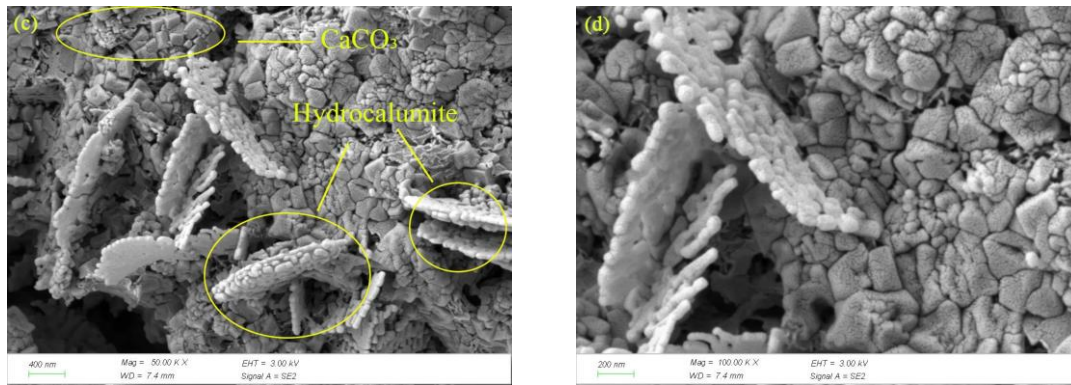


Fig. 13 Scanning electron micrograph of CNGA3 specimen 28d

436 As illustrated in Fig. 13, the CNGA3 specimen with 4% NDA and a 28 d compressive strength of 11.65 MPa exhibits
 437 obvious cracks and a loose overall structure. Hydration products are scattered and fail to form a dense network.
 438 Flaky crystals, presumed to be hydrocalumite, show high chemical stability but a loose structure with limited
 439 contribution to strength. Unlike the fibrous C–S–H network in CNGA1, no distinct C–S–H network is observed in
 440 CNGA3, indicating that excessive NDA may inhibit its formation. Numerous uniformly distributed granular
 441 particles are identified as calcite CaCO_3 , likely formed by early carbonation under high NDA content. No evident
 442 binding phase or dense filling is observed between particles, reflecting weak bonding performance.
 443 At high NDA dosage, substantial CaCO_3 forms from the carbonation of $\text{Ca}(\text{OH})_2$. Although chemically stable,
 444 CaCO_3 contributes little to strength and hinders C–S–H formation. Elevated NDA enhances Al_2O_3 reactivity,
 445 promoting hydrocalumite formation, but its loose flaky structure offers limited strength gain. Extensive cracks and
 446 pores are consistent with the low 28 d compressive strength of 11.65 MPa. The high porosity and loose structure
 447 markedly reduce CNGA3 strength. SEM shows a loose matrix with abundant granular calcite and flaky
 448 hydrocalumite, while a continuous C–S–H network is absent, accounting for the low compressive strength. A
 449 comparison between CNGA1 and CNGA3 is provided in Table 11.

Table 11 Comparison of CNGA1 and CNGA3 systems

Characteristics	CNGA1	CNGA3
Porosity	Low	High
Hydration Products	Dominated by C-S-H, with $\text{Ca}(\text{OH})_2$ as the secondary phase	Dominated by Calcite (CaCO_3) and Hydrocalumite
Microstructure	Dense	Loose with numerous cracks
28-day Compressive Strength	27.12MPa	11.65MPa

4. Conclusions

452 Through systematic macroscopic and microscopic analyses, this study investigates the hydration characteristics and
 453 reaction mechanisms of all-solid-waste cementitious materials prepared by activating a GGBS–BA precursor with
 454 a CS–NDA composite alkaline activator. Four key factors, namely alkaline solid waste ratio, NDA dosage, water-

455 to-binder ratio, and precursor proportion, were evaluated for their effects on workability, mechanical properties, and
456 microstructural evolution using XRD, FTIR, and SEM-EDS. The main conclusions are as follows:

457 1. In CNGA all-solid-waste cementitious materials, SO_4^{2-} reacts with C–A–H gel from GGBS hydration and Ca^{2+}
458 supplied by CS to preferentially form AFt. This AFt, with acicular or columnar morphology, interpenetrates the C–
459 S–H gel framework, enhancing mechanical interlocking and filling micropores between gel particles. Together,
460 these effects create a gel–crystal composite structure that serves as the primary source of strength.

461 2. The high-alkaline environment established by CN dual-alkaline synergistic activation enables a functional
462 division of alkali sources, featuring rapid alkalinity increase and sustained retention. An appropriate NDA dosage
463 provides highly active alkali, and the high solubility of Na^+ quickly raises the pH of the system. Meanwhile, CS acts
464 as a stable alkali reservoir, where $\text{Ca}(\text{OH})_2$ gradually dissolves to maintain long-term alkalinity and prevent sudden
465 pH decline. As a result, CN dual-alkaline activation overcomes the limitations of slow alkali development and
466 unstable alkalinity in single solid-waste systems.

467 3. CS contributes to strength development in CNGA all-solid-waste cementitious materials through both alkaline
468 activation and latent cementitious properties. It supplies OH^- to create a high-alkaline environment, breaking down
469 inert layers on GGBS and BA and promoting formation of C–S–H and AFt. It also provides abundant Ca^{2+} , which
470 reacts with SiO_3^{2-} and AlO_2^- to form C–(A)–S–H gel. In sulfate-containing systems, CS further reacts with sulfates
471 to generate limited AFt, aiding pore filling and microstructural densification.

472 4. NDA dosage significantly affects strength, with an optimal level of 2% balancing alkaline activation and
473 suppression of side reactions. This dosage enhances the hydration of GGBS and BA, promotes C–S–H formation,
474 and produces a small amount of CaCO_3 for pore filling, thereby improving strength. Excessive NDA is unfavorable,
475 as non-cementitious byproducts become dominant and hinder strength development.

476 5. CS provides the activation environment, NDA stabilizes it and regulates product types, GGBS supplies the main
477 cementitious products, and BA contributes reactive components to enhance chemical stability. Together, the CNGA
478 system forms an integrated control framework covering effective activation, stable reactions, cementitious product
479 formation, and dense structural development.

480 **CRedit authorship contribution statement**

481 Qiyue Ren: Data curation, Formal analysis, Investigation, Methodology, Visualization, Writing-original draft.

482 Yannian Zhang: Data curation, Formal analysis, Investigation, Methodology, Visualization, Writing-original draft,
483 Project administration, Funding acquisition. Yingliang Tan: Project administration, Supervision, Writing-original

484 draft, Funding acquisition. Qingjie Wang: Investigation, Supervision, Writing - review & editing. Moncef L. Nehdi:
485 Investigation, Supervision, Writing - review & editing. Shunshan Zhang: Investigation, Supervision, Writing -
486 review & editing.

487 **LLM Usage Declaration**

488 During the preparation of this manuscript, we used ChatGPT (OpenAI) solely for language polishing and
489 grammatical correction of the full text, to improve the readability and fluency of the English expression. The tool
490 was not used to generate any research content, design experiments, process or analyze experimental data, or interpret
491 research results. All scientific concepts, experimental designs, data analysis, research conclusions and core content
492 of this manuscript are the original work of the authors.

493 **Declaration of Competing Interest**

494 The authors declare that they have no known competing financial interests or personal relationships that could have
495 appeared to influence the work reported in this paper.

496 **Acknowledgments**

497 Funding: This work was supported by the Key Project of National Natural Science Foundation of China (No.
498 52234004), the Key Research and Development Project of the Science and Technology Plan of Liaoning Province-
499 Industrial Technology Innovation Category (No. 2024JH2/102400016), the Basic Research Project of the
500 Department of Education of Liaoning Province (LJ212510150005), and the Science and Technology Plan Project
501 of the Department of Housing and Urban-Rural Development of Liaoning Province (LNSJSKJ-2025-060).

502 **References**

- 503 [1] Y. Zhang, W. Liu, Q. Wang, L. Zhang, Coupling mechanisms and synergistic effects in portland cement-ceramic powder-ground
504 granulated blast furnace slag-CFB desulfurization ash composite binder [J], Waste and Biomass Valorization
505 (2025).<http://dx.doi.org/10.1007/s12649-025-03270-8>
- 506 [2] K. Kaptan, S. Cunha, J. Aguiar, A review: Construction and demolition waste as a novel source for CO₂ reduction in portland cement
507 production for concrete [J], Sustainability 16(2) (2024).<http://dx.doi.org/10.3390/su16020585>
- 508 [3] A. Alsalman, L.N. Assi, R.S. Kareem, K. Carter, P. Ziehl, Energy and CO₂ emission assessments of alkali-activated concrete and
509 ordinary portland cement concrete: A comparative analysis of different grades of concrete [J], Cleaner Environmental Systems 3
510 (2021).<http://dx.doi.org/10.1016/j.cesys.2021.100047>
- 511 [4] P. Kryvenko, I. Rudenko, P. Sikora, M. Sanytsky, O. Konstantynovskyi, T. Kropyvnytska, Alkali-activated cements as sustainable
512 materials for repairing building construction: A review [J], Journal of Building Engineering 90 (2024)
513 27.<http://dx.doi.org/10.1016/j.jobe.2024.109399>
- 514 [5] H.S. Gökçe, Durability of slag-based alkali-activated materials: A critical review [J], Journal of the Australian Ceramic Society
515 60(3) (2024) 885–903.<http://dx.doi.org/10.1007/s41779-024-01011-z>
- 516 [6] M.R. Ahmad, A. Fernández-Jimenez, B. Chen, Z. Leng, J.-G. Dai, Low-carbon cementitious materials: Scale-up potential,
517 environmental impact and barriers [J], Construction and Building Materials 455
518 (2024).<http://dx.doi.org/10.1016/j.conbuildmat.2024.139087>
- 519 [7] S. Sasui, G. Kim, A. van Riessen, H. Eu, J. Park, J. Nam, C. Lim, Effects of Na₂SiO₃/NaOH ratio in alkali activator on the

520 microstructure, strength and chloride ingress in fly ash and GGBS based alkali activated concrete [J], Journal of Building Engineering
521 98 (2024) 17.<http://dx.doi.org/10.1016/j.jobe.2024.111255>

522 [8] J. Chen, J. Plank, Alkali-activated calcined clay blended cement: Effect of NaOH activator on performance of HPEG PCEs and on
523 early strength [J], Cement and Concrete Research 183 (2024) 14.<http://dx.doi.org/10.1016/j.cemconres.2024.107588>

524 [9] X. Quan, G. Zhao, X. Liu, M. Bu, Investigation on the sodium silicate modulus-affected macroscopic and microscopic
525 characteristics of alkali-activated slag concrete [J], Materials Science and Technology (2025)
526 14.<http://dx.doi.org/10.1177/02670836241306659>

527 [10] S. Dueramae, W. Tangchirapat, P. Chindapasirt, C. Jaturapitakkul, P. Sukontasukkul, Autogenous and drying shrinkages of mortars
528 and pore structure of pastes made with activated binder of calcium carbide residue and fly ash [J], Construction and Building Materials
529 230 (2020) 9.<http://dx.doi.org/10.1016/j.conbuildmat.2019.116962>

530 [11] E. Adesanya, P. Perumal, T. Luukkonen, J. Yliniemi, K. Ohenoja, P. Kinnunen, M. Illikainen, Opportunities to improve
531 sustainability of alkali-activated materials: A review of side-stream based activators [J], Journal of Cleaner Production 286
532 (2021).<http://dx.doi.org/10.1016/j.jclepro.2020.125558>

533 [12] J. Oti, B.O. Adeleke, F.X. Anowie, J.M. Kinuthia, E. Ekwulo, Mechanical properties of a sustainable low-carbon geopolymer
534 concrete using a pumice-derived sodium silicate solution [J], Materials 17(8) (2024) 16.<http://dx.doi.org/10.3390/ma17081792>

535 [13] S.K. Tripathy, J. Dasu, Y.R. Murthy, G. Kapure, A.R. Pal, L.O. Filippov, Utilisation perspective on water quenched and air-cooled
536 blast furnace slags [J], Journal of Cleaner Production 262 (2020).<http://dx.doi.org/10.1016/j.jclepro.2020.121354>

537 [14] Y. Zheng, J. Wu, A. Yang, B. Li, L. Gu, Feasibility study on the one-part geopolymer activated by solid sodium silicate for soft
538 soil solidification [J], Rock and Soil Mechanics 45(07) (2024) 2072–2084.<http://dx.doi.org/10.16285/j.rsm.2023.1290>

539 [15] W. Guo, Q. Zhao, Y. Qiu, Y. Shi, S. Wang, Basic mechanical properties and stress-strain relationship of soda residue-calcium
540 carbide slag activated concrete [J], Materials Reports 38(17) (2024) 140–147.<http://dx.doi.org/10.11896/cldb.22070247>

541 [16] X. Gu, X. Li, Y. Zhao, J. Liu, Z. Hu, Z. Hu, Effect of desulfurization ash and carbide slag double-mixture on hydration of slag-
542 based cementitious materials [J], Metal Mine (02) (2025) 240–246.<http://dx.doi.org/10.19614/j.cnki.jsks.202502032>

543 [17] M.T. Marvila, A.R. Garcez de Azevedo, J.A. Tostes Linhares Júnior, C.M. Fontes Vieira, Activated alkali cement based on blast
544 furnace slag: Effect of curing type and concentration of Na₂O [J], Journal of Materials Research and Technology 23 (2023) 4551–
545 4565.<http://dx.doi.org/10.1016/j.jmrt.2023.02.088>

546 [18] X. Ji, Z. Wang, X. Wang, X. Zhao, H. Zhang, T. Zhang, Microstructures and properties of alkali-activated slags with composite
547 activator: Effects of Na₂O equivalents [J], Journal of Cleaner Production 450 (2024).<http://dx.doi.org/10.1016/j.jclepro.2024.141754>

548 [19] D. Xu, W. Ni, Q. Wang, C. Xu, Y. Jiang, Preparation of clinker-free concrete by using soda residue composite cementitious material
549 [J], Journal of Harbin Institute of Technology 52(08) (2020) 151–160.<http://dx.doi.org/10.11918/201909069>

550 [20] J. Seo, S. Park, H.N. Yoon, J.G. Jang, S.H. Kim, H.K. Lee, Utilization of calcium carbide residue using granulated blast furnace
551 slag [J], Materials 12(21) (2019).<http://dx.doi.org/10.3390/ma12213511>

552 [21] L. Wang, H. Chen, Y. Zhang, Study on mechanical properties and hydration characteristics of bauxite-GGBFS alkali-activated
553 materials, based on composite alkali activator and response surface method [J], Materials 18(7)
554 (2025).<http://dx.doi.org/10.3390/ma18071466>

555 [22] G. Yang, C. Li, W. Xie, Y. Yue, C. Kong, X. Li, Effect of carbide slag and steel slag as alkali activators on the key properties of
556 carbide slag-steel slag-slag-phosphogypsum composite cementitious materials [J], Frontiers in Materials 11
557 (2024).<http://dx.doi.org/10.3389/fmats.2024.1353004>

558 [23] Q. Fu, M. Bu, Z. Zhang, W. Xu, Q. Yuan, D. Niu, Hydration characteristics and microstructure of alkali-activated slag concrete:
559 A review [J], Engineering 20 (2023) 162–179.<http://dx.doi.org/10.1016/j.eng.2021.07.026>

560 [24] L. Liu, X. Chen, K. Pang, A. Neupane, L. Xie, D. Shen, Degradation of alkali-activated slag pastes exposed to high-concentration
561 chloride, sulfate and magnesium multi-salt solutions [J], Construction and Building Materials 464 (2025)
562 15.<http://dx.doi.org/10.1016/j.conbuildmat.2025.140182>

563 [25] Y. Gu, P. Dangla, R.-P. Martin, o. metalssi-omikrine, T. Fen-Chong, Modeling the sulfate attack induced expansion of cementitious

564 materials based on interface-controlled crystal growth mechanisms [J], Cement and Concrete Research 152 (2022)
565 15.<http://dx.doi.org/10.1016/j.cemconres.2021.106676>

566 [26] J. Zhu, H. Cui, L. Cui, S. Yang, C. Zhang, W. Liu, D. Zheng, Mutual activation mechanism of cement-GGBS-steel slag ternary
567 system excited by sodium sulfate [J], Buildings 14(3) (2024) 17.<http://dx.doi.org/10.3390/buildings14030631>

568 [27] J.M. Etchevery, Y.A. Villagran-Zaccardi, P. Van den Heede, V. Hallet, N. De Belie, Effect of sodium sulfate activation on the
569 early age behaviour and microstructure development of hybrid cementitious systems containing portland cement, and blast furnace slag
570 [J], Cement and Concrete Composites 141 (2023).<http://dx.doi.org/10.1016/j.cemconcomp.2023.105101>

571 [28] L. Zhang, Y. Zhang, Q. Wang, W. Zhang, Z. Li, Y. Shang, H.-Q. Sun, Effects of two activators on the hydration characteristics and
572 microstructure of lithium slag-steel slag-containing composite cementitious materials [J], Construction and Building Materials 483
573 (2025).<http://dx.doi.org/10.1016/j.conbuildmat.2025.141749>

574 [29] S. Zhang, Y. Zhang, J. Zhang, Y. Li, Compressive strength and resistance to sulphate attack of ground granulated blast furnace
575 slag, lithium slag, and steel slag alkali-activated materials [J], Buildings 14(8) (2024).<http://dx.doi.org/10.3390/buildings14082320>

576 [30] Y. Li, S. Duan, H. Wu, X. Shi, X. Han, P. Zhao, Z. Ma, Mechanical properties and hydration mechanism of red mud-fly ash-
577 calcium carbide slag composite cementitious materials [J], Bulletin of the Chinese Ceramic Society 44(03) (2025) 1041–
578 1049.<http://dx.doi.org/10.16552/j.cnki.issn1001-1625.2024.1104>

579 [31] H. Wang, X. Zhao, T. Wang, L. Su, B. Zhou, Y. Lin, Determination of gel products in alkali-activated fly ash-based composites
580 incorporating inorganic calcium additives [J], Advances in Materials Science and Engineering 2022 (2022) 1–
581 13.<http://dx.doi.org/10.1155/2022/7476671>

582 [32] Z. Li, K. Xu, N. Sun, J. Wang, K. Xue, L. Xu, Y. Ren, Z. Yan, T. Sima, Compressive strength and microstructure of carbide slag
583 and alkali-activated blast furnace slag pastes in china [J], Buildings 14(6) (2024).<http://dx.doi.org/10.3390/buildings14061681>

584 [33] GB/T 17671-2021, Method of testing cements-determination of strength (ISO method).2021
585